Evidence of Energy and Momentum Flux from Swell to Wind

KIMMO K. KAHMA

Marine Research, Finnish Meteorological Institute, Helsinki, Finland

MARK A. DONELAN AND WILLIAM M. DRENNAN

Rosenstiel School of Marine and Atmospheric Science, University of Miami, Miami, Florida

EUGENE A. TERRAY

Woods Hole Oceanographic Institution, Woods Hole, Massachusetts

(Manuscript received 30 October 2015, in final form 13 April 2016)

ABSTRACT

Measurements of pressure near the surface in conditions of wind sea and swell are reported. Swell, or waves that overrun the wind, produces an upward flux of energy and momentum from waves to the wind and corresponding attenuation of the swell waves. The estimates of growth of wind sea are consistent with existing parameterizations. The attenuation of swell in the field is considerably smaller than existing measurements in the laboratory.

1. Introduction

Our topic here is that of swell waves and their interaction with the atmospheric boundary layer. Here we define swell as waves traveling faster than the local wind. It has long been known that swell waves can have an influence on the momentum flux at the air–sea interface. Indeed, Volkov (1970) and Makova (1975) noted upward momentum fluxes in the presence of swell. These data were interpreted as evidence for a wave-coherent component of the velocity field (also Davidson and Frank 1973). More recent field observations showing an effect of swell on the air–sea momentum flux include those of Geernaert et al. (1988), Rieder (1997), Donelan et al. (1997), Drennan et al. (1999), Smedman et al. (1999, 2009), and Grachev and Fairall (2001). The consensus of data shows that swell in the presence of light to moderate winds can dramatically change the air–sea momentum flux over pure wind sea values, increasing it when the swell runs against the wind and reducing it, sometimes to zero or even to an opposite direction, when the swell travels with the wind.

Donelan (1990), Smedman et al. (1999, 2003, 2009), Högström et al. (2009, 2013, 2015), and others have shown that strong swells traveling faster than the wind can significantly alter the near-surface mean wind speeds from the logarithmic profiles expected over land or, in most conditions, over the sea. In extreme conditions, wind speeds were observed to be highest near the surface—the ‘‘wave-driven wind’’ phenomenon first noted by Harris (1966) in the laboratory.

These studies and others have provided a challenge to the modeling community to simulate the observed behavior. Recent model results (e.g., Kudryavtsev and Makin 2004; Hanley and Belcher 2008; Sullivan et al. 2008; Semedo et al. 2009) capture the main features discussed above, and at the same time allow for the study of the basic mechanisms by which swell waves influence the atmosphere. In general, the stress τ can be decomposed into three components: viscous stress τ_ν, turbulent stress τ_t, and a wave coherence stress τ_w:

$$\tau(z) = \tau_\nu(z) + \tau_t(z) + \tau_w(z). \qquad (1)$$

Here z is the height above the surface. Volkov (1970) recognized that swell waves must act on the atmosphere through τ_w, which at the surface takes the form

Denotes Open Access content.

Corresponding author address: Kimmo Kahma, Kehräkuja 3, FI-00730 Helsinki, Finland.
E-mail: kimmo.kahma@kolumbus.fi

DOI: 10.1175/JPO-D-15-0213.1

$\tau_w = \overline{p_o \partial\eta/\partial x}$, where p_o is the pressure at the surface and $\partial\eta/\partial x$ is the slope of the surface. This term, also known as the form drag, represents the momentum transfer from the wind field to the waves (in the case of wave growth) or vice versa (in the case of wave attenuation).

Likewise, the energy flux into surface waves is given by $\partial E/\partial t = -\overline{p_o \partial\eta/\partial t}$, where E is the wave energy density. Although considerable efforts have been expended over the decades in measuring the flux $\overline{p_o \partial\eta/\partial t}$ between waves and the atmosphere, it nevertheless remains one of the least well known fundamental quantities in air–sea interaction. This is in large part because p_o cannot be measured; instead, pressure must be measured at some distance above the surface and then extrapolated down. Even this is difficult, as the pressure field decays exponentially above the surface. The early field measurements of Dobson (1971), Elliott (1972b), and Snyder (1974) were reconciled by Snyder et al. (1981). Hsiao and Shemdin (1983), Hasselmann and Bösenberg (1991), Hristov et al. (1998), and Donelan et al. (2006) have reported more recent field measurements. Most frequently reported are dimensionless wave growth rates, which we define as

$$\zeta(\omega) = \frac{1}{\omega S_{\eta\eta}(\omega)} \frac{\partial S_{\eta\eta}(\omega)}{\partial t}, \tag{2}$$

where $S_{\eta\eta}$ is the power spectrum of $\eta(t)$. We note that this dimensionless wave growth parameter ζ, originally defined by Miles (1957), is equal to the β parameter of Kahma (1981) and is related to the dimensionless growth parameter γ of Snyder et al. (1981) by $\zeta = (\rho_a/\rho_w)\gamma$ (here ρ_a, ρ_w are the air and water densities) and to the dimensional β parameter of Plant (1982) by $\zeta = \beta/\omega$.

For growing wave conditions $U/c > 1$, where U is the wind speed (subscripts to U refer to the measuring height) and c is the wave phase speed, the wave growth has been found to scale as

$$\zeta = (0.2 \text{ to } 0.3)(\rho_a/\rho_w)(U_5/c - 1) \tag{3}$$

using field data (Snyder et al. 1981), or based on both field and laboratory data (Plant 1982)

$$\zeta = (0.04 \pm 0.02)(u_*/c)^2 \cos\theta, \tag{4}$$

where $u_* = \sqrt{\tau/\rho_a}$ is the friction velocity and θ is the difference in direction between waves and wind, or

$$\zeta = 0.28(\rho_a/\rho_w)(U/c - 1)|U/c - 1| \tag{5}$$

according to Donelan (1999), using laboratory data with winds referenced to half a wavelength of the waves.

As yet, wave growth measurements over swell $U/c < 1$ in the field are very sparse. The few cases of Snyder et al. (1981) showed $\zeta \approx 0$ over fast waves. Hasselmann and Bösenberg (1991) reported no significant growth or attenuation over swell waves, that is, ζ not significantly different from zero. Hristov et al. (1998) reported a few cases with $\partial E/\partial t = -\overline{p_o \partial\eta/\partial t} < 0$ over fast-moving swell waves ($U_{10}/c < 0.25$), but not enough data were collected to allow for anything more than a qualitative interpretation.

Several laboratory studies have investigated the attenuation rates of paddle waves traveling against the wind. While attenuation rates of opposing swell were also found to scale as either $(U/c - 1)|U/c - 1|$ (Young and Sobey 1985; Donelan 1999) or $(u_*/c)^2$ (Peirson et al. 2003), an additional quadratic dependence on swell steepness ak was found (Young and Sobey 1985):

$$\zeta = (-0.7 \pm 0.02)(\rho_a/\rho_w)(ak)^2(1 - U_\infty/c)^2, \tag{6}$$

where a and k are the amplitude and the wavenumber, and U_∞ is the free-stream velocity.

The various studies report a wide range of attenuation rates. Donelan (1999) reported attenuation rates roughly half the amplitude of wind sea growth rates, while Young and Sobey (1985) reported even lower attenuation rates at swell steepnesses typical of ocean conditions. Peirson et al. (2003) reported attenuation rates larger than Donelan's by a factor of 3.

Makin et al. (2007), in one of the few studies of paddle-generated waves traveling in the wind direction, report a strong dependence of the stress distribution on wave steepness, with total stress decreasing for low ak. They did not report attenuation rates of the paddle-generated waves, as their particular focus was on the interaction of the paddle- and wind-generated waves. However, they do point out several differences between swell waves in the ocean and their paddle-generated counterparts. Paddle-generated waves are much shorter than ocean swells and closer in peak frequency to the wind sea, and so are likely to be more strongly coupled to the wind sea waves. For this reason the strong interaction between paddle waves and wind waves seen in the laboratory (e.g., Mitsuyasu 1966; Phillips and Banner 1974; Donelan 1987) is not usually observed in the ocean (see also Chen and Belcher 2000). The shorter paddle waves have phase speeds much lower than ocean swells, and usually less than the wind speed. Only at sea does the situation exist where swell waves are significantly faster than the wind. Hence, the analogy of laboratory conditions with those in the field breaks down in the conditions of following swell.

In the absence of field measurements, and without an appropriate analogy in the laboratory, attenuation rates in following swells are still unknown. This was identified by Semedo et al. (2009) as a key need for their modeling efforts. The recent renewal of interest in the topics of wave growth and swell (Högström et al. 2013, 2015) recalled to our attention an experiment performed some years ago. During this experiment, conducted from a tower in Lake Ontario, pressure and wave slope measurements were made in a variety of sea states, including following swell. In section 2 we describe the experiment, and in section 3 we present the data. In section 4 we report estimates of energy and momentum flux along with growth rates ζ from these measurements. In section 5 we put our results in the context of the earlier studies.

2. Experiment

The data discussed here were collected during autumn 1987 as part of the Water–Air Vertical Exchange Study (WAVES), conducted from an offshore tower in Lake Ontario. The tower, situated in 12-m water, 1.1 km from the western shore of the lake, is operated by the Canada Centre for Inland Waters, Burlington, Ontario. During the WAVES experiment, the tower was instrumented to measure waves, currents, meteorology, turbulence in the lake and atmosphere, and pressure. A detailed description of the experiment, including photographs of the tower and of many sensors, is found in Donelan et al. (1999). See also Terray et al. (1996) and Drennan et al. (1999), where other findings from WAVES are presented.

We describe briefly the sensors of particular interest in this paper. Static pressure above the surface was measured using Elliott probes (Elliott 1972a). These disks of 40 mm diameter and 3 mm thickness are specially designed and machined to eliminate dynamic pressure effects from the probe itself on the pressure field. The pressure ports from the disk are led to one side of a differential pressure transducer (MKS Baratron model 233AH), and also to the other side through a pneumatic low-pass filter. The effect is to high pass the pressure signal and thus to remove spurious contributions longer than $O(1000)$ s. The probes, as well as the extensive calibration and response correction procedures, are further discussed in Donelan et al. (1999).

Three static Elliott probes were mounted with the disks in the vertical plane on a vaned profiler on the northeast leg of the tower (see Fig. 1). Spacing between the probes was 1 m, and the elevation of the lowest probe from the mean water level varied between 1 and 3.9 m. The height of the profiler was adjusted at the start of each run to keep the lowest probe above the waves, but as close to them as possible. The height of the probes was fixed for the duration of each run, avoiding the need for the additional corrections required for pressure measurements in a surface-following frame (e.g., Donelan et al. 2006).

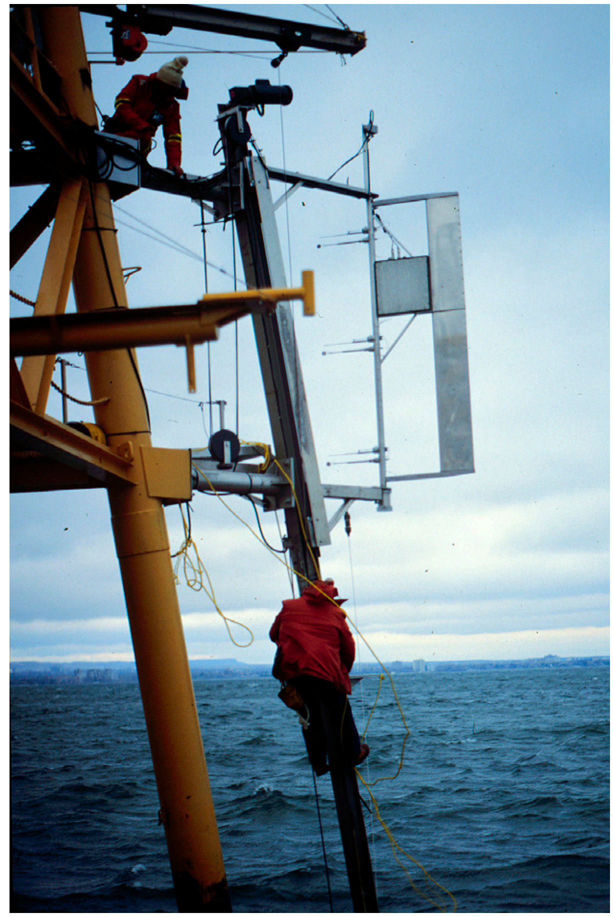

FIG. 1. Photograph of northeast leg of WAVES tower showing vane with pressure probes (Elliotts and Pitots) taken during installation.

A capacitance wave wire mounted near the wave profiler was used for surface elevation measurements. The 0.5–0.9-m horizontal distance from the pressure sensors to the wave wire, which varied according to the heading of the vane, was corrected using the calculated phase angles associated with the appropriate wavenumber. Wave data were analyzed for significant wave height and peak frequency ω_p. In addition, directional wave spectra were calculated using the maximum likelihood method on data from an array of six wave wires arranged in a centered pentagon of a 0.25-m radius.

Figure 2 shows sample signals of the three Elliott pressure sensors, along with the surface elevation. Figures 2a and 2c show a case of growing waves, whereas Figs. 2b and 2d show the high coherence found in the presence of swell.

Finally, wind speed and direction, as well as wind stress, were measured using a Gill bivane anemometer on a mast at 12 m. Drennan et al. (1999) discussed the processing associated with the bivane data. All data

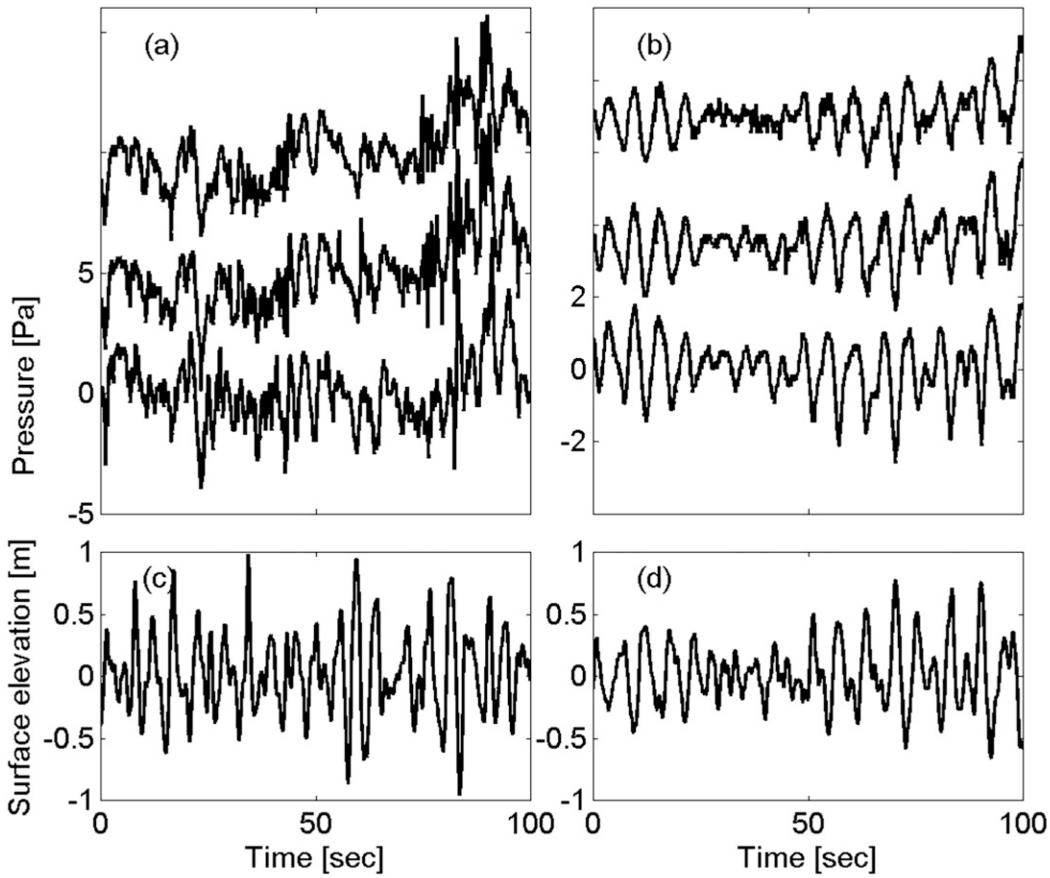

FIG. 2. Times series of (top) pressure and (bottom) surface elevation η for (a),(c) wind sea run 87128 and (b),(d) swell run 87146. Each plot shows three pressure curves, one from each of the Elliott probes, with the lowest/highest probe at the bottom/top. The probe spacing is 1 m, with the lowest probe at 1.87 m above mean water level for each run.

discussed here were sampled at 20 Hz and processed in runs of 13–90 min. For several of the runs, wind stress data are not available.

3. Data processing

To reduce any possible distortion effects of the tower on the flow recorded by the Elliott probes, only winds from the open northeast quadrant are used. Other criteria for the wind are stationarity and a speed sufficient to force the wind profiler vane ($U_{12} > 3\,\mathrm{m\,s^{-1}}$). These conditions are much more restrictive than those used in earlier WAVES analyses, and they significantly reduce the size of the dataset to 51 runs.

To simplify the problem, we require that the angle between mean wind direction Θ_U and peak wave direction Θ_w be less than 25° and that the waves have unimodal (self-similar) wave spectra. This eliminates the need to explicitly account for directional effects. Whatever they are, they will, under these assumptions, be accounted for in the dependence of the flux and the growth rate on U/c. About half of the runs meet the directionality criteria; of these, 8 had to be rejected because the pressure sensor was not functioning properly (purging, out of range, etc.; see Donelan et al. 1999 for details).

Nineteen runs meet these stringent criteria. Nine of the runs can be classified as wind sea, with inverse wave ages U_{12}/c_p around 1.1. One case represents fully developed waves, with U_{12}/c_p around 0.8. The other nine cases are swell dominated, with U_{12}/c_p between 0.42 and 0.61. Here we use the measured wind speed at 12 m, and not the standard 10-m wind speed, as the height adjustment has been shown to be questionable in swell-dominated conditions (Drennan et al. 1999). The adjustment, at any rate, could be applied to wind sea cases only, would be small, and would not change the classification (wind sea or swell) of any run. Further quality criteria were applied to the individual frequency components for these runs, as described below.

TABLE 1. Parameters of accepted runs (method 2; see section 3) showing inverse wave age U_{12}/c_p, phase angle between lowest pressure and surface elevation integrated over the spectrum ϕ [degrees; see Eq. (10)], height of the lowest pressure sensor z (m), significant wave height H_s (m), peak wave frequency f_p (Hz), mean 12-m wind speed U_{12} and standard deviation σ_U (m s^{-1}), wind direction mean Θ_U and standard deviation σ_Θ (degrees), air and water temperatures T_a and T_w (°C), peak wave direction Θ_w (degrees), and friction velocity u_* (m s^{-1}).

Run	U_{12}/c_p	ϕ	z	H_s	f_p	U_{12}	σ_U	Θ_U	σ_Θ	T_a	T_w	Θ_w	u_*
						Wind sea							
87032	1.18	222	1.04	0.32	0.39	4.77	0.57	25.8	9.5	3.88	7.13	35	—
87035	1.35	205	1.28	0.76	0.27	7.71	0.81	74.7	7.9	−0.09	6.78	60	0.20
87036	1.10	194	1.71	0.85	0.23	7.28	0.78	59.5	8.9	−0.13	6.76	50	—
87116b	1.13	206	3.85	2.38	0.13	10.83	1.37	52.8	4.5	3.07	5.07	60	0.28
87128a	1.15	219	1.87	1.40	0.18	9.52	1.00	80.0	6.4	2.23	4.52	65	0.35
87128b	1.14	207	1.87	1.40	0.18	9.45	1.00	80.0	6.4	2.23	4.52	65	0.35
87128c	1.21	210	1.87	1.40	0.18	10.05	1.00	80.0	6.4	2.23	4.52	65	0.35
87130	1.09	201	2.58	1.45	0.17	9.39	0.93	77.6	6.7	1.99	4.46	60	0.41
87132a	1.21	229	2.07	1.75	0.15	10.81	1.15	76.1	5.9	0.88	4.47	60	0.37
87132b	1.16	229	2.08	1.75	0.15	10.37	1.15	76.1	5.9	0.88	4.47	60	0.37
87132c	1.11	225	2.08	1.75	0.15	9.93	1.15	76.1	5.9	0.88	4.47	60	0.37
						Fully developed							
87127a	0.74	179	1.45	0.73	0.19	5.86	0.78	73.8	7.7	1.60	4.69	60	0.22
87127b	0.80	172	1.43	0.73	0.19	6.31	0.78	73.8	7.7	1.60	4.69	60	0.22
87127c	0.85	193	1.42	0.73	0.19	6.71	0.78	73.8	7.7	1.60	4.69	60	0.22
						Swell							
87056a	0.53	170	1.21	0.66	0.20	3.99	0.49	42.2	5.9	7.04	6.85	50	0.10
87056b	0.59	176	1.20	0.66	0.20	4.42	0.49	42.2	5.9	7.04	6.85	50	0.10
87056c	0.61	173	1.19	0.66	0.20	4.62	0.49	42.2	5.9	7.04	6.85	50	0.10
87057	0.47	178	1.45	0.79	0.21	3.38	0.29	45.8	3.7	7.05	6.83	50	0.08
87058	0.43	178	1.65	0.85	0.18	3.46	0.58	46.2	4.2	7.07	6.83	55	0.07
87126	0.56	170	1.47	0.70	0.18	4.59	0.60	62.5	7.1	1.21	4.73	70	0.12
87135	0.59	176	3.89	1.22	0.14	5.40	0.40	63.9	2.7	4.98	3.98	50	—
87138	0.61	169	1.69	1.25	0.17	5.25	0.40	60.7	3.1	5.36	4.02	55	0.15
87139	0.60	175	2.65	1.37	0.17	5.15	0.54	51.3	9.9	5.15	4.04	55	0.17
87146a	0.48	179	1.86	1.13	0.15	4.21	0.31	75.5	4.7	5.49	4.30	60	—
87146b	0.42	179	1.87	1.13	0.15	3.76	0.31	75.5	4.7	5.49	4.30	60	—
87146c	0.44	182	1.87	1.13	0.15	3.86	0.31	75.5	4.7	5.49	4.30	60	—
87147	0.55	176	3.18	1.10	0.17	4.67	0.36	77.4	4.1	5.13	4.32	60	—

To ensure sufficient stability of the spectral estimates, wide bin width was used. To verify the robustness of the results, we calculated the spectra with two methods: method 1 uses the full run length with 200 degrees of freedom, while method 2 uses half-hour segments (or the run length in the few cases when the run is shorter) with 100 degrees of freedom. To keep the degrees of freedom fixed in both methods (and consequently all points of equal weight) the bin width was wider for the short runs. This means that the bin width considerably varies in method 1, whereas there are only few runs in method 2, where the bin is wider than $\Delta\omega = 0.35\,\mathrm{rad\,s^{-1}}$. Method 1 shows somewhat less scatter but has also far fewer points, and therefore the confidence limits for Eq. (11), for example, are wider in method 1 than in method 2. The results and conclusions are similar from both methods.

In line with the simplifying requirement of a unimodal directional wave spectrum aligned with the wind, we use only frequency components from $0.7\omega_p$ to $2\omega_p$, that is, around the peak of the wave spectrum. We refer to this as method 2a. In a subset we have used the components at the peak wave frequency only; this is referred as method 2b. The runs that have accepted bins according to method 2a are listed in Table 1.

To find the energy flux, we first calculate the cross-spectrum $S_{p\eta}(\omega)$. The extrapolation of pressure fluctuations from the measurement height z to the water surface was done assuming the decay of e^{-kz} predicted by classical potential flow theory. Here, k is the wavenumber associated with ω.

The spectrum of energy flux to waves will then be

$$-\mathrm{Im}S_{p\eta}(\omega)e^{kz}\omega, \tag{7}$$

where the flux is defined to be negative when the flux is downward and the wave spectrum would potentially be increasing with time. The actual rate of change of the wave spectrum depends besides wind input also on the other source terms of the energy balance equation; a small downward flux could therefore even be cancelled by dissipation. As usual, we will determine the

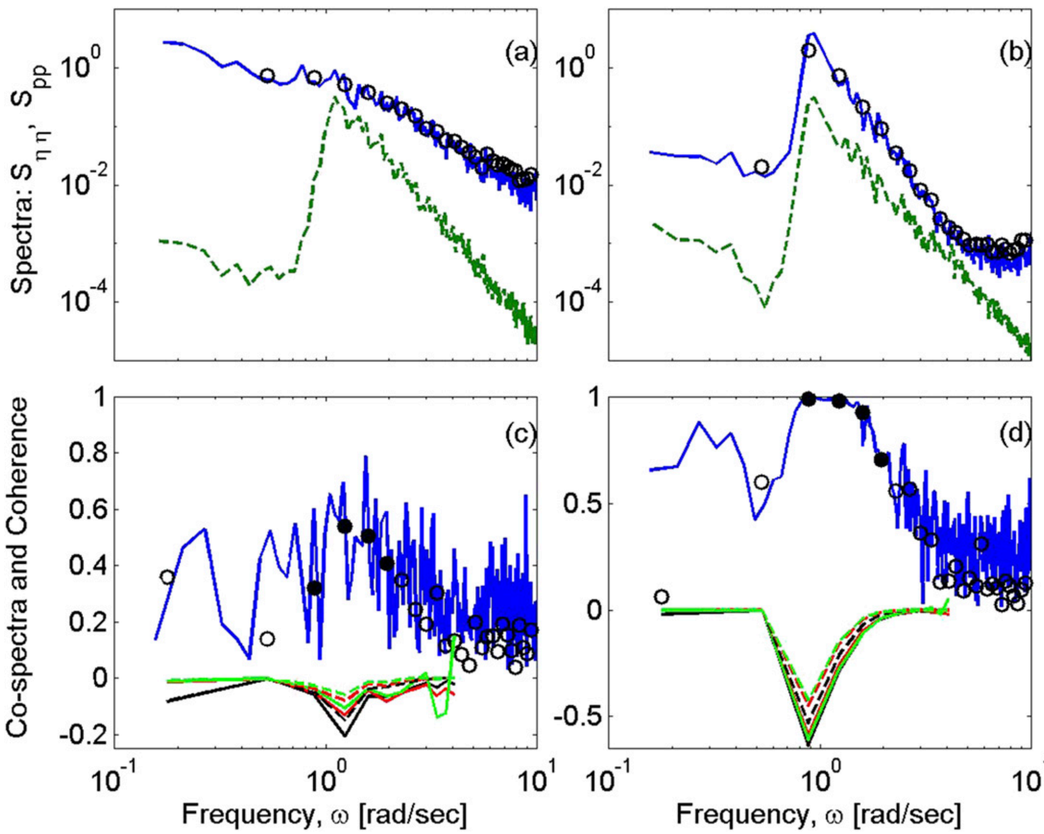

FIG. 3. Sample spectra from (a),(c) wind sea run 87128 and (b),(d) swell run 87146. (top) Spectra of lowest Elliott probe pressure p [without height adjustment (blue lines) and adjusted (open circles); Pa^2 rad^{-1} s] and surface elevation η (dashed; m^2 rad^{-1} s). (bottom) Coherence between p and η without adjustment (blue lines) and adjusted (open circles) pressure. The black/red/green lines show $\mathrm{Re}S_{p\eta}$ for the lowest/middle/highest pressure probes, where the solid lines include a $\exp(kz)$ height adjustment for p. The filled circles indicate the frequencies where the data passed all quality controls.

dimensionless growth rate ζ defined by Eq. (2), assuming that the other terms except the input source term and the rate of change of the spectrum term of the energy balance equation vanish. The dimensionless growth rate ζ for a particular frequency component will then be

$$\zeta(\omega) = \frac{\mathrm{Im}S_{p\eta}(\omega)e^{kz}}{\rho_w g S_{\eta\eta}(\omega)}. \quad (8)$$

Figure 3 shows the cospectrum $\mathrm{Co}(\omega) = \mathrm{Re}S_{p\eta}(\omega)$ both without any height adjustment and with the $\exp(kz)$ adjustment. For the swell cases (e.g., run 87146 shown in Figs. 3b,d) near the peak of the wave spectrum, when the coherence between p and η is near one (Fig. 3b), the adjustment brings the fluxes from the different pressure sensors together. For higher frequencies the extrapolation of the pressure to the surface magnifies the noise: see, for instance, Fig. 3c, where the height-adjusted flux cospectra diverge for $\omega > 3\,\mathrm{rad\,s^{-1}}$, with the highest probe (green curve) showing the largest errors. We therefore have accepted data only from the wavenumbers where the extrapolation is reasonable. The limit of extrapolation was set to 2.7, that is, when $kz < 1$. The phase shift between the pressure sensors was usually less than 10 degrees, and it varied randomly with a small bias (pressure at the higher level leading the lower; cf. Tables 2, 3). Henceforth, we use only the lowest pressure sensor for each run in calculating fluxes and growth rates. To reduce the noise from this source, we required, as in Snyder et al. (1981), that the maximum phase shift between the lowest two pressure sensors was less than 15°. In addition, we required that the coherence between p and η is twice the mean noise level of the coherence found in the high-frequency part of the spectrum. Note that for the wind sea cases (e.g., run 87128 shown in Figs. 3a,c) the coherence between p and η is much lower than during swell. Some of the runs meeting the general criteria have no bins that meet the bin criteria, usually because the coherence does not rise sufficiently above the noise level. The runs that have accepted bins are listed in Table 1.

TABLE 2. Parameters of accepted frequency bins for wind sea cases based on the lowest Elliot pressure probe E1. The columns are run number, inverse wave age $U_{12}/c(\omega)$; growth rate $\zeta/(1 \times 10^{-4})$ calculated from Eq. (8); energy flux (mW m^{-2}) calculated from Eq. (7) integrated over the spectral bin width $\Delta\omega = 0.35$ rad s^{-1}; height adjustment $\exp(kz)$, where k is wavenumber; phase angle between E1 and middle Elliott probe E2 ϕ_{12} (degrees, where positive means E1 leads E2); coherence (%) between pressure p and surface elevation η; phase angle between p and η (degrees); and slope ak, $a^2 = 2S_{\eta\eta}(\omega)\Delta\omega$ from the spectral bin width $\Delta\omega = 0.35$ rad s^{-1}.

Run	U_{12}/c	ζ	Energy flux	$\exp(kz)$	ϕ_{12}	Coherence	$\phi_{p\eta}$	ak
87032	0.94	−0.02	0.01	1.5	−7.3	35	179.6	0.0108
87032	1.12	−1.02	2.55	1.7	−2.1	41	145.2	0.0253
87035	1.47	1.10	−24.01	1.6	−6.5	57	211.4	0.0546
87035	2.05	1.08	−8.78	2.4	−12.4	52	195.8	0.0553
87036	1.29	0.66	−22.03	1.7	−1.0	49	205.7	0.0606
87116b	1.13	0.40	−93.00	1.4	−2.4	34	210.9	0.0693
87128a	1.02	0.36	−4.19	1.2	−10.0	33	195.0	0.0156
87128a	1.24	0.56	−38.16	1.4	2.0	39	215.0	0.0537
87128a	1.55	1.51	−61.70	1.6	−11.1	59	231.9	0.0591
87128a	1.88	2.78	−51.83	2.1	0.4	60	230.4	0.0538
87128b	1.02	0.16	−1.65	1.2	−3.0	42	185.4	0.0145
87128b	1.23	0.36	−22.67	1.4	−0.9	47	199.6	0.0517
87128b	1.53	0.61	−28.80	1.6	3.3	34	213.8	0.0634
87128b	1.87	0.73	−13.64	2.0	−0.7	35	200.3	0.0539
87128c	1.08	0.49	−9.07	1.2	−5.9	42	196.6	0.0197
87128c	1.31	0.99	−82.05	1.4	−6.6	64	210.6	0.0594
87128c	1.63	1.59	−59.80	1.6	−3.6	48	232.1	0.0567
87128c	1.99	1.86	−44.08	2.1	0.5	61	209.2	0.0606
87130	1.22	0.53	−38.12	1.5	−3.9	45	207.2	0.0555
87130	1.53	1.25	−39.94	1.9	−0.2	39	229.9	0.0522
87132	1.16	1.04	−69.55	1.2	−9.0	57	215.3	0.0373
87132a	1.41	1.20	−81.76	1.4	−7.3	35	245.9	0.0540
87132a	1.75	2.22	−76.35	1.7	−0.3	37	259.9	0.0542
87132b	1.11	1.03	−124.67	1.2	−8.3	66	219.4	0.0501
87132b	1.35	1.78	−204.22	1.4	0.8	68	246.7	0.0699
87132b	1.68	1.93	−59.79	1.7	−8.2	40	234.1	0.0514
87132c	1.29	1.12	−87.55	1.4	−4.2	52	231.0	0.0579
87132c	1.61	2.61	−98.48	1.7	−12.5	58	245.4	0.0568

The total energy flux

$$\overline{p_o \partial\eta/\partial t} = \int_0^\infty -\mathrm{Im}S_{p\eta}(\omega)e^{kz}\omega\, d\omega \tag{9}$$

cannot be directly calculated from our data because the noise level induced by the height adjustment renders $-\mathrm{Im}S_{p\eta}(\omega)e^{kz}\omega$ essentially useless for frequencies much higher than ω_p. As an indicator, we have calculated for each run without height adjustment the integrated phase shift ϕ between pressure p at the lowest height and η:

$$\tan(\phi) = \frac{\int_0^\infty -\mathrm{Im}S_{p\eta}(\omega)\omega\, d\omega}{\int_0^\infty \mathrm{Re}S_{p\eta}(\omega)\omega\, d\omega}. \tag{10}$$

This phase shift ϕ in Table 1 is consistently over 180° for the wind sea cases $U_{12}/c_p > 1$, suggesting downward flux from wind to waves. For eight of the nine swell cases, ϕ is less than or equal to 180°, suggesting upward flux.

4. Results

The growth rates ζ and energy fluxes in growing wind sea are shown in Table 2. The flux calculated for a specific bin is multiplied by $\Delta\omega = 0.35$ rad s^{-1} so as to represent the integral contribution. A downward flux is defined to be negative, and an upward flux positive. Table 2 also shows the height extrapolation factor that starts from a modest 10% increase up to the acceptance criterion of 170% increase. In agreement with the findings of Snyder et al. (1981), the phase shift between the two lowest pressure sensors is random with essentially zero mean. No statistically significant dependence on $U_{12}/c(\omega)$, height, or coherence could be seen. The coherence between pressure and surface elevation is low in the growing sea cases as turbulence dominates the wave coherent flow at the measuring elevations. In the presence of swell, in contrast, the coherence is very high (almost 1) near the swell frequencies. This is also evident in the wind velocity spectra plotted in Fig. 4. Note especially the collapse of turbulence in the vertical wind component over swell (Fig. 4b). For reference, an $\omega^{-5/3}$

TABLE 3. Parameters of accepted frequency bins for swell cases. For definitions, see Table 2.

Run	U_{12}/c	ζ	Energy flux	$\exp(kz)$	ϕ_{12}	Coherence	$\phi_{p\eta}$	ak
87056a	0.52	−0.46	3.24	1.2	−9.7	88	173.4	0.0174
87056a	0.65	−0.27	3.24	1.4	−9.1	84	175.5	0.0320
87056a	0.72	−0.23	2.42	1.4	−11.8	76	174.5	0.0300
87056c	0.55	−0.61	1.61	1.2	−13.2	81	170.1	0.0089
87056c	0.65	−0.22	3.13	1.3	−2.4	86	175.7	0.0282
87056c	0.78	−0.06	0.59	1.4	3.5	70	178.2	0.0311
87057	0.44	−0.17	4.01	1.3	0.4	98	178.1	0.0315
87057	0.52	0.28	−5.45	1.4	0.4	96	183.3	0.0379
87057	0.61	−0.22	2.17	1.6	−10.7	88	177.1	0.0347
87057	0.71	−0.61	4.32	1.9	−10.5	82	169.7	0.0361
87058	0.38	−0.47	0.16	1.2	−1.5	66	175.6	0.0027
87058	0.45	0.02	−0.64	1.3	0.6	97	180.3	0.0351
87058	0.56	0.02	−0.33	1.5	−1.6	93	180.3	0.0363
87058	0.69	0.03	−0.33	1.9	−5.9	81	180.5	0.0396
87126	0.50	0.06	−0.17	1.2	−3.7	65	181.0	0.0078
87126	0.60	−0.13	2.10	1.3	−0.3	81	177.3	0.0263
87126	0.74	−0.02	0.16	1.5	−6.1	39	179.4	0.0256
87135	0.69	−0.13	4.89	1.8	−5.4	85	176.5	0.0383
87138	0.57	−0.20	5.47	1.2	3.2	95	175.7	0.0240
87138	0.69	−0.50	22.51	1.3	−0.9	93	168.6	0.0439
87138	0.85	−0.02	0.22	1.5	−1.3	78	179.6	0.0330
87138	1.04	−0.68	7.25	1.9	−1.5	61	163.0	0.0407
87139	0.56	−0.24	11.64	1.3	3.2	92	174.8	0.0318
87139	0.67	−0.01	0.32	1.5	−5.2	87	179.8	0.0438
87139	0.84	0.10	−1.88	2.0	−7.4	65	182.1	0.0404
87146a	0.46	0.09	−3.20	1.2	4.5	98	181.2	0.0281
87146a	0.55	0.23	−6.89	1.4	5.2	97	183.2	0.0362
87146a	0.68	−0.35	6.17	1.6	5.3	92	174.9	0.0386
87146b	0.41	−0.21	7.15	1.2	1.9	99	177.4	0.0271
87146b	0.49	−0.09	2.84	1.4	1.7	98	178.9	0.0371
87146b	0.61	0.15	−1.96	1.6	1.4	93	181.9	0.0339
87146c	0.40	0.21	−1.21	1.2	−3.0	95	182.9	0.0098
87146c	0.46	0.08	−3.64	1.3	1.2	98	181.1	0.0362
87146c	0.54	0.21	−4.62	1.4	3.2	97	183.0	0.0353
87146c	0.66	0.58	−3.70	1.7	0.4	88	188.4	0.0249
87147	0.51	−0.22	9.29	1.4	−2.3	97	176.2	0.0300
87147	0.61	−0.26	6.61	1.7	0.4	92	175.5	0.0328
87147	0.76	0.03	−0.34	2.3	−3.8	77	180.5	0.0340

line representing the expected inertial subrange behavior of isotropic turbulence is also plotted. Significantly reduced shear-generated turbulence levels in the presence of swell have been reported in, for example, Drennan et al. (1999) and Smedman et al. (1999). This can be explained by looking at the fluxes of energy.

Examples of the energy flux are shown in Fig. 5. In run 87128a representing growing wind seas, the flux is downward for the frequency bins where $U_{12}/c(\omega) > 1$ (Fig. 5a). In the fully developed run 87127, the flux is downward when $U_{12}/c(\omega) > 1$ and upward when $U_{12}/c(\omega) < 1$ (Fig. 5b). In the swell-dominated run 87126a (Fig. 5c), the flux is upward.

Figure 6a shows the growth rates in the frequency bins $0.7\omega_p, \ldots, 2\omega_p$ around the peak ω_p, and Fig. 6b shows the growth rates when the bin at ω_p is used. From Table 2 we can see that in the case of a growing sea Fig. 5a is representative for all the bins except one. Of the 12 fully developed bins, one bin shows a downward flux when $U_{12}/c(\omega) < 1$, and the others agree with Fig. 5b (Table 4). Table 2 shows that in a growing sea the phase shift between pressure and elevation is usually much more over 180° than the phase shift between the two pressure sensors. If there is any bias, it will be small compared with magnitude of the flux.

In swell-dominated cases the fluxes are much smaller, and there is more scatter. The energy flux of 2/3 of the bins in Table 3 is upward when half hour sections are used (method 2a; see section 3). In most cases the downward flux is small, and the dataset is consistent with the uncertainty in the extrapolation to the surface as inferred from the statistics of the phase angle difference between the two lowest pressure sensors. When analyzed by method 1, which has more degrees of freedom

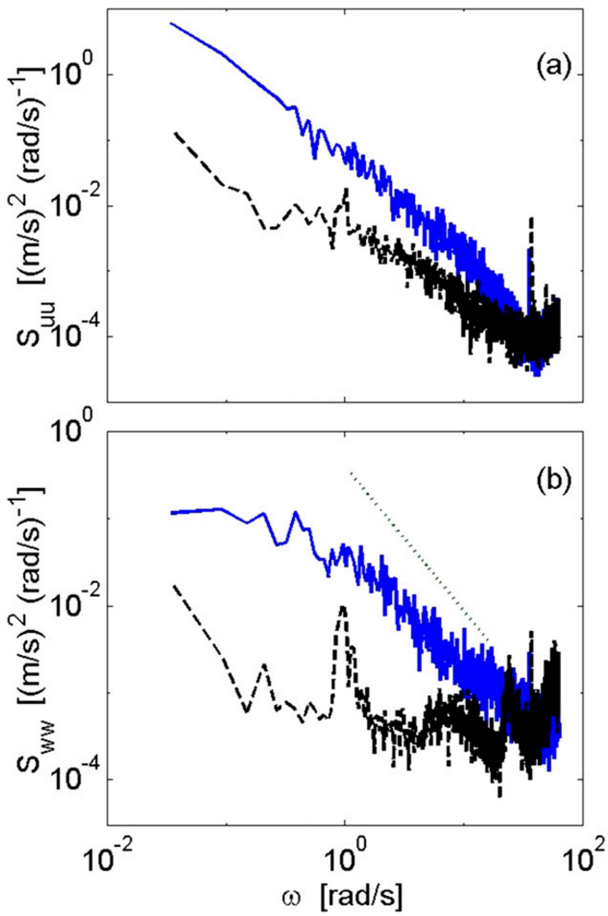

FIG. 4. Spectra of (a) horizontal and (b) vertical wind velocities for wind sea run 87128 (solid) and swell run 87146 (dashed). The dotted line in (b) shows an $\omega^{-5/3}$ inertial subrange line.

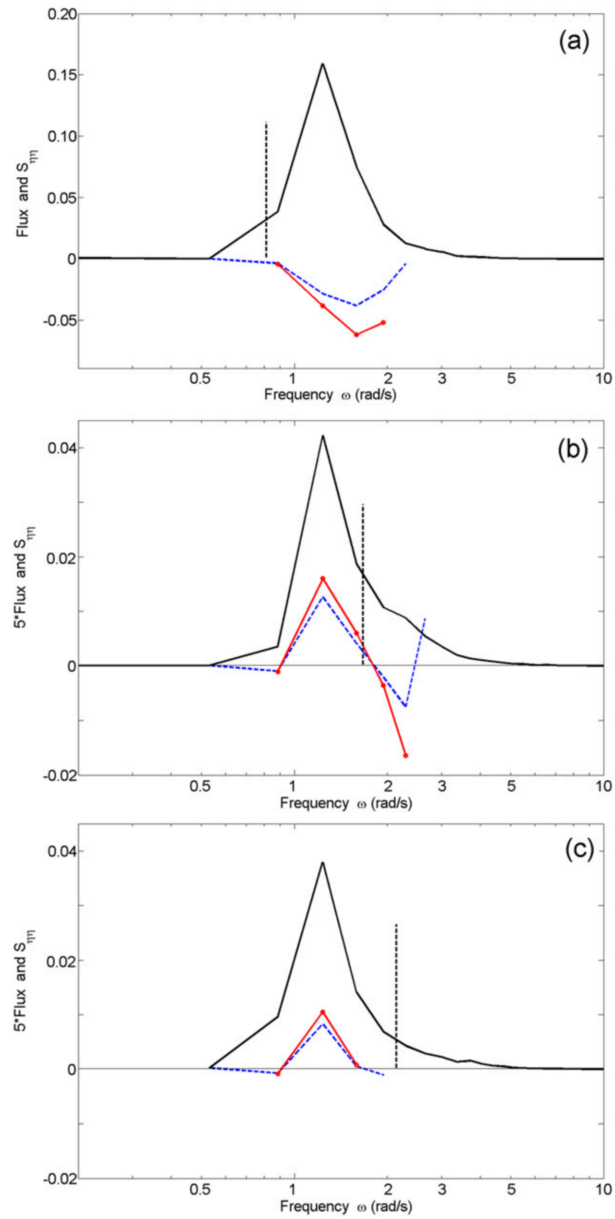

FIG. 5. Surface elevation spectrum $S_{\eta\eta}$ (m^2 rad^{-1} s; solid black line), calculated energy flux (W m^{-2}) without the exp(kz) adjustment (dashed blue line), and energy flux in accepted bins adjusted by exp(kz) (solid red line with dots). (a) Wind sea run 87128, (b) fully developed run 87127, and (c) swell run 87126. The vertical dashed lines indicate the frequency where $U_{12} = c(\omega)$. Note the different scales and gain factors multiplying flux in the panels.

per bin, 87% of the bins have an upward flux, again in agreement with the statistics of the phase angle difference. Tables 2–4 show that the pressure signal at the higher elevation leads the lower one by about 3 degrees on average. Although this difference is not statistically significant, it still suggests that our estimates of the upward flux during swell are more likely to be underestimated than overestimated. This strengthens our case for an upward flux when $U_{12}/c(\omega) < 1$.

This difference between a growing sea and swell can be seen also when the pressure measurements at higher elevations are considered. Although the coherence between pressure and surface elevation is low in case of growing sea, all three pressure measurements show consistent fluxes in 15 of the 16 half hour segments, as well as in all the three segments of fully developed run 87127. In Fig. 6a, which shows the growth rate as a function of $U_{12}/c(\omega)$, the cases in which fluxes are consistent are distinguished by circles around the symbols. Only a single point of the 49 bins in a growing or fully developed sea is without a circle in Fig. 6a. The trimmed mean (12 most deviating points excluded) of the ratio of the fluxes calculated from the middle versus the bottom pressure sensor is 0.97.

In swell-dominated conditions the situation is again different. While the coherence is high between pressure and surface elevation, the fluxes are consistent only in

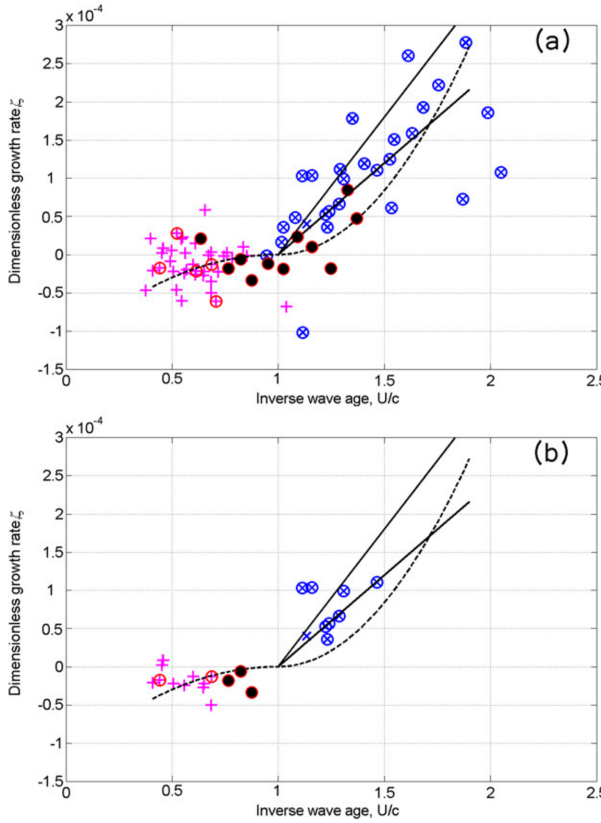

FIG. 6. Dimensionless growth rate ζ vs inverse wave age $U_{12}/c(\omega)$. (a) Growth rates in the frequency bins $0.7\omega_p, \ldots, 2\omega_p$ around the peak ω_p and (b) growth rates when the bin at ω_p is used. Wind sea runs are indicated by $\times$, swell runs by $+$, and fully developed sea runs by bullets. The runs in which fluxes calculated from different elevations are consistent at some range around ω_p are distinguished by circles around the symbols: blue for wind sea and red for swell and fully developed sea. The solid lines represent the spread of the Snyder et al. (1981) data; the dashed lines are the curves of Donelan (1999).

2 of the 13 half-hour segments. Only 5 of the 38 points in swell-dominated conditions have circles in Fig. 6a. The trimmed mean (18 most deviating points excluded) of the ratio of the fluxes calculated from the middle versus bottom pressure sensor is now only 0.86. These differences seem to be a real physical phenomenon related to the presence of swell rather than a change in other environmental parameters or an instrumentation problem, since the fluxes in a swell-dominated run 87126 are not consistent, whereas in run 87127, begun only 1 h after run 87126 was completed, the fluxes are consistent. No indication of any instrumental malfunction can be seen between these runs.

The same conclusions hold for the momentum flux estimates, which for individual frequency bins are given by energy flux over phase speed. In the presence of swell the downward momentum flux at high frequencies [those with $U_{12}/c(\omega) > 1$] can be cancelled by the upward momentum flux at the lower (swell) frequencies. The resultant total flux is near zero, or even upward in extreme cases, as first noted by Volkov (1970), and so is the friction velocity, which represents the scale of shear-generated turbulence. This explains the high coherence between pressure and waves reported above in swell conditions.

5. Discussion

In the case of growing waves, our growth rates in Fig. 6a (method 2a) are within the range of the relations derived from earlier experiments, and despite the large scatter, the positive correlation of ζ with $[U_{12}/c(\omega) - 1]$ is statistically significant at well over 99% confidence level. When the linear relation is forced through $\zeta(1) = 0$, it takes the form

$$\zeta = (2.4 \times 10^{-4} \pm 0.3 \times 10^{-4})[U_{12}/c(\omega) - 1], U_{12}/c(\omega) > 1, \tag{11}$$

or alternatively,

$$\zeta = (0.21 \pm 0.02)(\rho_a/\rho_w)[U_{12}/c(\omega) - 1], U_{12}/c(\omega) > 1. \tag{12}$$

Results from method 1 are statistically consistent with method 2, but have wider confidence limits. If a quadratic form (Donelan 1999) is used instead, we find

$$\zeta = 0.21(\rho_a/\rho_w)[U_{12}/c(\omega) - 1]|U_{12}/c(\omega) - 1|, U_{12}/c(\omega) > 1. \tag{13}$$

The linear relation [Eq. (3)] proposed by Snyder et al. (1981) is closer to our data than the quadratic relation [Eq. (5)] of Donelan (1999), but both are within the scatter of our data.

In the case of swell there is no statistically significant correlation between ζ and $U_{12}/c(\omega)$. To be sure that our main result, the upward flux in case of swell, is robust, we calculated the mean value of the decay rate for swell in three different ways. Method 1 and method 2b (data in Fig. 6b) both give the mean value of decay rate for swell -0.17×10^{-4}. The 67% confidence limits are largest, 0.06×10^{-4} in case of method 1. In Methods 2a and 2b, confidence limits are the same, 0.04×10^{-4}, but the mean value is -0.1×10^{-4} in the case of method 2a (data in Fig. 6a). All these values are statistically consistent and the difference from zero is statistically significant in all three methods at the 99% confidence level at least.

TABLE 4. Parameters of accepted frequency bins for fully developed cases. For definitions, see Table 2.

Run	U_{12}/c	ζ	Energy flux	$\exp(kz)$	ϕ_{12}	Coherence	$\phi_{p\eta}$	ak
87127a	0.63	0.21	−0.22	1.1	−13.6	40	184.6	0.0047
87127a	0.76	−0.18	3.20	1.3	1.4	78	175.4	0.0277
87127a	0.95	−0.12	1.20	1.5	−8.6	52	175.6	0.0295
87127a	1.16	0.10	−0.72	1.7	−3.7	41	184.4	0.0333
87127a	1.37	0.47	−3.29	2.2	−2.5	32	197.6	0.0421
87127b	0.82	−0.06	0.87	1.3	−8.2	59	177.8	0.0252
87127b	1.02	−0.19	1.67	1.4	2.5	58	174.5	0.0275
87127b	1.25	−0.18	1.55	1.7	−7.0	31	169.9	0.0365
87127c	0.88	−0.34	5.27	1.3	−1.9	54	166.9	0.0259
87127c	1.09	0.24	−2.90	1.4	−3.3	53	188.6	0.0324
87127c	1.33	0.85	−8.62	1.7	−11.0	35	226.5	0.0397

The data do not suggest a quadratic relation for swell. If we use it for comparison anyway, the coefficient 0.03 in the quadratic relation

$$\zeta = 0.03(\rho_a/\rho_w)[U_{12}/c(\omega) - 1]|U_{12}/c(\omega) - 1|, U_{12}/c(\omega) < 1 \quad (14)$$

is a fit to the data in a least squares sense. The residual when the relation is subtracted from the data does not show any statistically significant trend or obvious curvature, and therefore the quadratic relation is not excluded by the data. If the quadratic relation were valid, the measured decay rate of following swell would be nearly an order of magnitude smaller than the growth rate, and also much smaller than the one reported by Donelan (1999) in the laboratory for swell against the wind.

Figure 7 shows the growth rate as a function of u_*/c. In the case of growing waves, our growth rates are consistent with Eq.(4) (Plant 1982), but for swell they show the attenuation that Eq.(4) does not predict.

The additional dependence on swell slope ak that Young and Sobey (1985) found in laboratory conditions could not be either verified or excluded by our data. The slope ak was calculated from the integrated wave energy over fixed spectral bin width $\Delta\omega = 0.35\,\mathrm{rad\,s^{-1}}$ by $a^2 = 2S_{\eta\eta}(\omega)\Delta\omega$. The growth rate ζ does not reveal any relations when plotted simultaneously against ak and $U_{12}/c(\omega)$. By taking advantage of the factorial form of Eq. (6), one can study first the dependence of $\zeta/(ak)^2$ on $[U_{12}/c(\omega) - 1]|U_{12}/c(\omega) - 1|$. The inverse wave age dependence predicted by Eq. (6) cannot be seen in the swell region (Fig. 8a), but there is a clear transition when $U_{12} = c(\omega)$. The picture is even more clear when the bins at ω_p are used only (Fig. 8b). We can then look at the dependence of $\zeta/\{[U_{12}/c(\omega) - 1]|U_{12}/c(\omega) - 1|\}$ on slope $(ak)^2$. No obvious relation can be seen (Fig. 9). We have calculated the straight line from Eq. (6), assuming that the coefficient would be consistent with the quadratic relation Eq. (13) at the mean of the $(ak)^2$ in our dataset. [The original coefficient −0.7 in Eq. (6) cannot be compared directly, as it refers to the amplitude of a monochromatic wave in laboratory conditions.] From Fig. 9 we conclude that the data do not suggest the slope dependence of Eq. (6), but it cannot be ruled out either.

Figure 5b shows how the energy flux changes its sign when the wave phase speed exceeds the wind speed U_{12}. We note also that in Fig. 6a no inverse wave age $U_{12}/c(\omega)$ other than 1 could serve better as the transition point from upward to downward flux. This is in agreement with Eqs. (3), (5), and (6), and in contradiction with Eq. (4). The experimental results showing nearly constant velocity profile in swell-dominated conditions (Högström et al. 2013, 2015) remove the need to take into account the elevation of U.

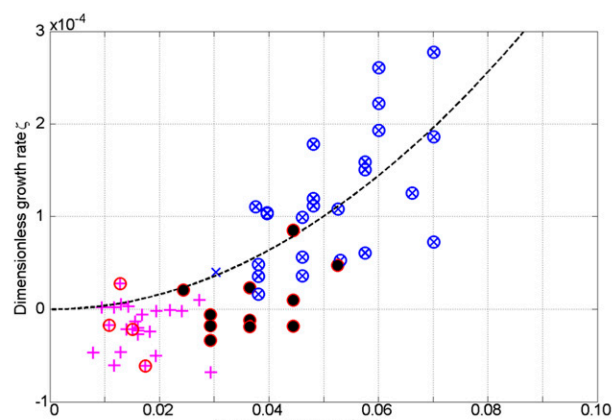

FIG. 7. Dimensionless growth rate ζ vs inverse wave age u_*/c, where u_* is the friction velocity and c is the phase speed. The growth rates are from frequency bins $0.7\omega_p, \ldots, 2\omega_p$ around the peak ω_p. Wind sea runs are indicated by ×, swell runs by +, and fully developed sea runs by bullets. The runs in which fluxes are consistent around ω_p are distinguished by circles around the symbols: blue for wind sea and red for swell and fully developed sea. The dashed line is Plant (1982).

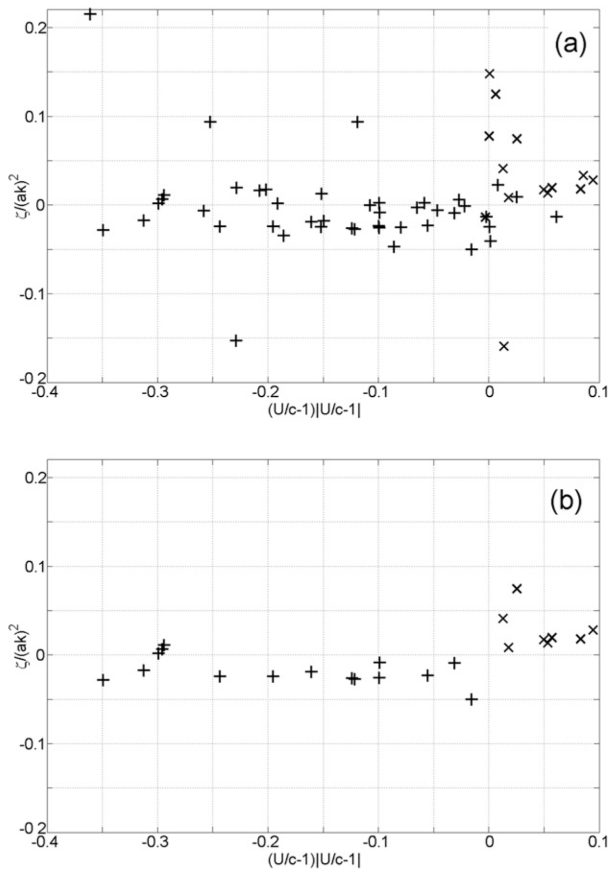

FIG. 8. Dimensionless growth rate scaled by slope squared $[\zeta/(ak)^2]$ as a function of $[U_{12}/c(\omega) - 1]|U_{12}/c(\omega) - 1|$. (a) Growth rates in the frequency bins $0.7\omega_p, \ldots, 2\omega_p$ around the peak ω_p and (b) growth rates when the bin at ω_p is used. Wind sea runs are indicated by $\times$, swell runs and fully developed sea runs by $+$. There are three outliers in (a) that are out of range of the figure; the absolute value of the flux for these outliers is less than $2\,\mathrm{mW\,m^{-2}}$.

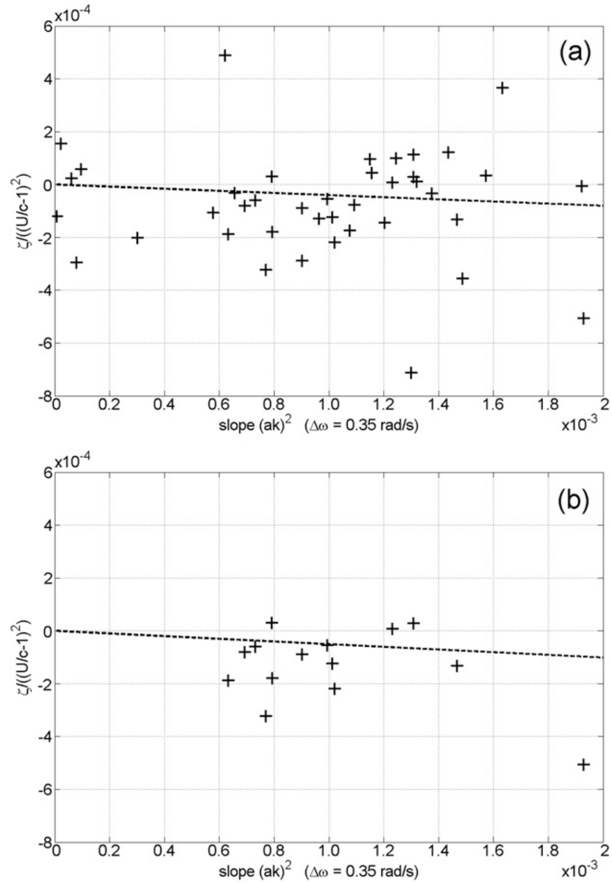

FIG. 9. Dimensionless growth rate scaled by $(U/c(\omega) - 1)^2$ as a function of slope squared. (a) Growth rates in the frequency bins $0.7\omega_p, \ldots, 2\omega_p$ around the peak and (b) growth rates when the bin at ω_p is used. Wind sea runs are indicated by $\times$, swell runs and fully developed sea runs by $+$. The dashed line is from Eq. (6) assuming that the coefficient would be consistent with the quadratic relation Eq. (13) at the mean of the $(ak)^2$ in our dataset. There are two outliers in (a) and one in (b) that are out of range of the figure; these cannot be removed by requiring that the flux is over $2\,\mathrm{mW\,m^{-2}}$.

When wind sea and swell are separated within the wave spectrum, the common practice up to now has been to use $U_{19.5}/c = 0.82$ or $U_{10}/c = 0.78$ as the inverse wave age that divides swell and wind sea. Our results call this practice into question and suggest instead that $U/c(\omega) = 1$ is the correct value, at least when wind and swell directions are close.

In our analysis, we have used only the frequency bins $0.7\omega_p, \ldots, 2\omega_p$ in the peak region. In the low-frequency part, the directional spreading increases below $0.7\omega_p$ and the unidirectional assumption is no longer valid. In the high-frequency part, the height adjustment magnifies the noise. Our analysis suggests that in the presence of swell we also have additional reasons for this restriction. In growing sea cases the fluxes outside this region $0.7\omega_p, \ldots, 2\omega_p$ show larger scatter but behave in a predictable way, provided that the other criteria are fulfilled. In swell-dominated runs the fluxes and growth rates outside the peak region are inconsistent with all the wave growth mechanisms and their Eqs. (3)–(6). The decay rate in swell-dominated runs is largest when the phase speed equals the wind speed $[U_{12}/c(\omega) = 1]$, and it is reduced to zero as the inverse wave age approaches 0.5. This trend is much reduced when only bins near the peak are used and disappears when only the flux at ω_p is used (Fig. 6b). We speculate that the reason for this is the complex interaction between the airflow and swell waves revealed in Högström et al. (2013, 2015). Far from the peak, the interaction between the airflow and wave components could be very different from the simplified theory of a single monochromatic wave under turbulent flow.

6. Conclusions

We have measured directly the growth and decay rate of waves in the field using wave and pressure measurements. The growth rate of wind sea waves $[U_{12}/c(\omega) > 1]$ agrees well with previous measurements. The decay rate of swell moving in the wind direction $[U_{12}/c(\omega) < 1]$ is statistically significant, but does not show any obvious dependence on $U_{12}/c(\omega)$, whereas the growth rate clearly increases with $U_{12}/c(\omega)$. Neither quadratic nor linear growth can be verified or excluded by the data.

The analysis of these data reveals that we are still far from having satisfactory field evidence about energy and momentum fluxes between swell and the atmosphere. During the past 30 years, only three experiments have data on pressure fluctuations above swell. Hasselmann and Bösenberg (1991) reported no significant growth or attenuation over swell waves. Hristov et al. (1998) had a few cases of upward flux over swell waves, but the data do not allow more than a qualitative interpretation. The data presented here are the first field measurements of pressure–wave correlation to show an upward flux during swell at over 99% confidence level, but we are still unable to determine whether quadratic or linear growth is correct, or to verify or reject the slope dependence observed in the laboratory. Analyzing the measurements using numerical modeling of the flow above waves might prove the way to make progress.

The analysis also shows that using the value of the inverse wave age $U_{19.5}/c = 0.82$ or $U_{10}/c = 0.78$ as the dividing line between swell and a wind sea, as has commonly been done, may not be correct. We suggest that $U/c(\omega) = 1$ is a better value, at least when the directions of wind and swell are close.

Acknowledgments. We gratefully acknowledge the contribution of many members of the engineering and technical staff of NWRI, Burlington in the design, construction, and operation of the apparatus, in particular D. Beesley, Y. Desjardins, R. Desrosiers, N. Madsen, M. Pedrosa, H. Savile, and J. Valdmanis.

REFERENCES

Chen, G., and S. E. Belcher, 2000: Effects of long waves on wind-generated waves. *J. Phys. Oceanogr.*, **30**, 2246–2256, doi:10.1175/1520-0485(2000)030<2246:EOLWOW>2.0.CO;2.

Davidson, K. L., and A. J. Frank, 1973: Wave-related fluctuations in the airflow above natural waves. *J. Phys. Oceanogr.*, **3**, 102–119, doi:10.1175/1520-0485(1973)003<0102:WRFITA>2.0.CO;2.

Dobson, F. W., 1971: Measurements of atmospheric pressure on wind-generated sea waves. *J. Fluid Mech.*, **48**, 91–127, doi:10.1017/S0022112071001496.

Donelan, M. A., 1987: The effect of swell on the growth of wind waves. *Johns Hopkins APL Tech. Dig.*, **8**, 18–23.

——, 1990: Air-sea interaction. *Ocean Engineering Science*, B. LeMéhauté and D. Hanes, Eds., The Sea—Ideas and Observations on Progress in the Study of the Seas, Vol. 9, John Wiley and Sons, 239–292.

——, 1999: Wind-induced growth and attenuation of laboratory waves. *Wind-over-Wave Couplings: Perspectives and Prospects*, S. G. Sajjadi, N. H. Thomas, and J. C. R. Hunt, Eds., Oxford University Press, 183–194.

——, W. M. Drennan, and K. B. Katsaros, 1997: The air–sea momentum flux in conditions of mixed wind sea and swell. *J. Phys. Oceanogr.*, **27**, 2087–2099, doi:10.1175/1520-0485(1997)027<2087:TASMFI>2.0.CO;2.

——, N. Madsen, K. K. Kahma, I. K. Tsanis, and W. M. Drennan, 1999: Apparatus for atmospheric surface layer measurements over waves. *J. Atmos. Oceanic Technol.*, **16**, 1172–1182, doi:10.1175/1520-0426(1999)016<1172:AFASLM>2.0.CO;2.

——, A. V. Babanin, I. R. Young, and M. L. Banner, 2006: Wave-follower field measurements of the wind-input spectral function part ii: Parameterization of the wind input. *J. Phys. Oceanogr.*, **36**, 1672–1689, doi:10.1175/JPO2933.1.

Drennan, W. M., K. Kahma, and M. Donelan, 1999: On momentum flux and velocity spectra over waves. *Bound.-Layer Meteor.*, **92**, 489–515, doi:10.1023/A:1002054820455.

Elliott, J. A., 1972a: Instrumentation for measuring static pressure fluctuations within the atmospheric boundary layer. *Bound.-Layer Meteor.*, **2**, 476–495, doi:10.1007/BF00821550.

——, 1972b: Microscale pressure fluctuations measured within the lower atmospheric boundary layer. *J. Fluid Mech.*, **53**, 351–384, doi:10.1017/S0022112072000199.

Geernaert, G. L., K. L. Davidson, S. E. Larsen, and T. Mikkelson, 1988: Wind stress measurements during the tower ocean wave and radar dependence experiment. *J. Geophys. Res.*, **93**, 13 913–13 923, doi:10.1029/JC093iC11p13913.

Grachev, A. A., and C. W. Fairall, 2001: Upward momentum transfer in the marine boundary layer. *J. Phys. Oceanogr.*, **31**, 1698–1711, doi:10.1175/1520-0485(2001)031<1698:UMTITM>2.0.CO;2.

Hanley, K. E., and S. E. Belcher, 2008: Wave-driven wind jets in the marine atmospheric boundary layer. *J. Atmos. Sci.*, **65**, 2646–2660, doi:10.1175/2007JAS2562.1.

Harris, D. L., 1966: The wave-driven wind. *J. Atmos. Sci.*, **23**, 688–693, doi:10.1175/1520-0469(1966)023<0688:TWDW>2.0.CO;2.

Hasselmann, D., and J. Bösenberg, 1991: Field measurements of wave-induced pressure over wind-sea and swell. *J. Fluid Mech.*, **230**, 391–428, doi:10.1017/S0022112091000848.

Högström, U., A. S. Smedman, E. Sahlée, W. M. Drennan, K. K. Kahma, H. Pettersson, and F. Zhang, 2009: The atmospheric boundary layer during swell: A field study and interpretation of the turbulent kinetic energy budget for high wave ages. *J. Atmos. Sci.*, **66**, 2764–2779, doi:10.1175/2009JAS2973.1.

——, A. Rutgersson, E. Sahlée, A. S. Smedman, T. S. Hristov, W. M. Drennan, and K. K. Kahma, 2013: Air-sea interaction features in the Baltic Sea and at a pacific trade wind site: An intercomparison study. *Bound.-Layer Meteor.*, **147**, 139–163, doi:10.1007/s10546-012-9776-8.

——, E. Sahlée, A. S. Smedman, A. Rutgersson, E. Nilsson, K. K. Kahma, and W. M. Drennan, 2015: Surface stress over the ocean in swell-dominated conditions during moderate winds. *J. Atmos. Sci.*, **72**, 4777–4795, doi:10.1175/JAS-D-15-0139.1.

Hristov, T. S., C. Friehe, and S. Miller, 1998: Wave-coherent fields in air flow over ocean waves: identification of cooperative behavior buried in turbulence. *Phys. Rev. Lett.*, **81**, 5245–5248, doi:10.1103/PhysRevLett.81.5245.

Hsiao, S. V., and O. H. Shemdin, 1983: Measurements of wind velocity and pressure with a wave follower during Marsen. *J. Geophys. Res.*, **88**, 9841–9849, doi:10.1029/JC088iC14p09841.

Kahma, K. K., 1981: A study of the growth of the wave spectrum with fetch. *J. Phys. Oceanogr.*, **11**, 1503–1515, doi:10.1175/1520-0485(1981)011<1503:ASOTGO>2.0.CO;2.

Kudryavtsev, V. N., and V. K. Makin, 2004: Impact of swell on the marine atmospheric boundary layer. *J. Phys. Oceanogr.*, **34**, 934–949, doi:10.1175/1520-0485(2004)034<0934:IOSOTM>2.0.CO;2.

Makin, V. K., H. Branger, W. L. Peirson, and J. P. Giovanangeli, 2007: Stress above wind-plus-paddle waves: Modeling of a laboratory experiment. *J. Phys. Oceanogr.*, **37**, 2824–2837, doi:10.1175/2007JPO3550.1.

Makova, V. I., 1975: Features of the dynamics of turbulence in the marine atmospheric surface layer at various stages in the development of waves. *Izv., Atmos. Ocean. Phys.*, **11**, 297–307.

Miles, J. W., 1957: On the generation of waves by shear flows. *J. Fluid Mech.*, **3**, 185–204, doi:10.1017/S0022112057000567.

Mitsuyasu, H., 1966: Interactions between water waves and wind (1). *Rep. Inst. Appl. Mech. Kyushu Univ.*, **14**, 67–88.

Peirson, W. L., A. W. Garcia, and S. E. Pells, 2003: Water wave attenuation due to opposing wind. *J. Fluid Mech.*, **487**, 345–365, doi:10.1017/S0022112003004750.

Phillips, O. M., and M. L. Banner, 1974: Wave breaking in the presence of wind drift and swell. *J. Fluid Mech.*, **66**, 625–640, doi:10.1017/S0022112074000413.

Plant, W. J., 1982: A relationship between stress and wave slope. *J. Geophys. Res.*, **87**, 1961–1967, doi:10.1029/JC087iC03p01961.

Rieder, K. F., 1997: Analysis of sea-surface drag parameterizations in open ocean conditions. *Bound.-Layer Meteor.*, **82**, 355–377, doi:10.1023/A:1000289415922.

Semedo, A., O. Saetra, A. Rutgersson, K. K. Kahma, and H. Pettersson, 2009: Wave induced wind in the marine boundary layer. *J. Atmos. Sci.*, **66**, 2256–2271, doi:10.1175/2009JAS3018.1.

Smedman, A. S., U. Högström, H. Bergström, A. Rutgersson, K. K. Kahma, and H. Pettersson, 1999: A case study of air-sea interaction during swell conditions. *J. Geophys. Res.*, **104**, 25 833–25 852, doi:10.1029/1999JC900213.

——, X. Guo Larsén, U. Högström, K. K. Kahma, and H. Pettersson, 2003: Effect of sea state on the momentum exchange over the sea during neutral conditions. *J. Geophys. Res.*, **108**, 3367, doi:10.1029/2002JC001526.

——, U. Högström, E. Sahlée, W. M. Drennan, K. K. Kahma, H. Pettersson, and F. Zhang, 2009: Observational study of marine atmospheric boundary layer characteristics during swell. *J. Atmos. Sci.*, **66**, 2747–2763, doi:10.1175/2009JAS2952.1.

Snyder, R. L., 1974: A field study of wave-induced pressure fluctuations above surface gravity waves. *J. Mar. Res.*, **32**, 497–531.

——, F. W. Dobson, J. A. Elliot, and R. B. Long, 1981: Array measurements of atmospheric pressure fluctuations above gravity waves. *J. Fluid Mech.*, **102**, 1–59, doi:10.1017/S0022112081002528.

Sullivan, P. P., J. B. Edson, T. Hristov, and J. C. McWilliams, 2008: Large eddy simulations and observations of atmospheric marine boundary layers above non-equilibrium surface waves. *J. Atmos. Sci.*, **65**, 1225–1245, doi:10.1175/2007JAS2427.1.

Terray, E. A., M. A. Donelan, Y. C. Agrawal, W. M. Drennan, K. K. Kahma, A. J. Williams III, P. A. Hwang, and S. A. Kitaigorodskii, 1996: Estimates of kinetic energy dissipation under breaking waves. *J. Phys. Oceanogr.*, **26**, 792–807, doi:10.1175/1520-0485(1996)026<0792:EOKEDU>2.0.CO;2.

Volkov, Y. A., 1970: Turbulent flux of momentum and heat in the atmospheric surface layer over a disturbed sea-surface. *Izv., Atmos. Ocean. Phys.*, **6**, 770–774.

Young, I. R., and R. J. Sobey, 1985: Measurements of the wind-wave energy flux in an opposing wind. *J. Fluid Mech.*, **151**, 427–442, doi:10.1017/S0022112085001033.